Enhancing co-production of H[subscript 2] and Syngas via Water Splitting and POM on Surface-Modified Oxygen Permeable Membranes

Citation: Wu, Xiao-Yu, Ahmed F. Ghoniem, and Mruthunjaya Uddi. "Enhancing Co-Production of H[subscript 2] and Syngas via Water Splitting and POM on Surface-Modified Oxygen Permeable Membranes." AIChE Journal 62, no. 12 (October 10, 2016): 4427–4435.

As Published: http://dx.doi.org/10.1002/aic.15518

Publisher: Wiley Blackwell

Persistent URL: http://hdl.handle.net/1721.1/109280

Version: Author's final manuscript: final author's manuscript post peer review, without publisher's formatting or copy editing

Enhancing co-production of H_2 and syngas via water splitting and POM on surface-modified oxygen permeable membranes[1]

Xiao-Yu Wu [a*], Mruthunjaya Uddi [b], Ahmed F. Ghoniem [a†]

[a] Department of Mechanical Engineering, Massachusetts Institute of Technology, 77 Massachusetts Avenue, Cambridge, MA 02139, USA

[b] Department of Mechanical Engineering, The University of Alabama, Room SERC 3072B Tuscaloosa, AL 35487, USA

Email address: * xywu@mit.edu (X.Y. Wu), † ghoniem@mit.edu (A.F. Ghoniem)

[1] This work is invited to submit as a "Best Paper Initiative" paper in AIChE Journal by Dr. Dushyant Shekhawat (National Energy Technology Laboratory). It was identified by Dr. Shekhawat as the Best Presentation in the session “Fuel Processing for Hydrogen Production” of the 2015 AIChE Annual Meeting in Salt Lake City.

Abstract

In this paper, we report a detailed study on co-production of H_2 and syngas on $La_{0.9}Ca_{0.1}FeO_{3-\delta}$ (LCF-91) membranes via water splitting and partial oxidation of methane (POM), respectively. A permeation model shows that the surface reaction on the sweep side is the rate limiting step for this process on a 0.9 mm-thick dense membrane at 990^{o}C. Hence, sweep side surface modifications such as adding a porous layer and nickel catalysts were applied; the hydrogen production rate from water thermolysis is enhanced by two orders of magnitude to 0.37 μmol/cm^2•s compared with the results on the unmodified membrane. At the sweep side exit, syngas (H_2/CO = 2) is produced and negligible solid carbon is found. Yet near the membrane surface on the sweep side, methane can decompose into solid carbon and hydrogen at the surface, or it may be oxidized into CO and CO_2, depending on the oxygen permeation flux.

Key words

MIEC, water splitting, thermolysis, POM, catalyst, hydrogen, membrane reactor

Introduction

Syngas, a mixture of H_2 and CO, is an important feedstock for the production of synthetic fuels and chemicals, such as methanol and ammonia which are among the top ten chemicals produced annually in the world[1,2]. Each chemical requires an optimum syngas composition in terms of the H_2/CO ratio[3]. Four approaches have been used to produce syngas from methane; each results in a unique H_2/CO ratio:

(1) Dry reforming (H_2/CO ratio = 1)

$$CH_4 + CO_2 \leftrightarrow 2CO + 2H_2 \qquad \Delta H_{298}^0 = 247 kJ/mol \qquad (1)$$

(2) Partial oxidation (H_2/CO ratio = 2)

$$CH_4 + \frac{1}{2}O_2 \leftrightarrow CO + 2H_2 \qquad \Delta H_{298}^0 = -36 kJ/mol \qquad (2)$$

(3) Steam reforming (H_2/CO ratio = 3)

$$CH_4 + H_2O \leftrightarrow CO + 3H_2 \qquad \Delta H_{298}^0 = 206 kJ/mol \qquad (3)$$

(4) Autothermal reforming (H_2/CO ~ 2.15)

$$CH_4 + 0.425O_2 + 0.15H_2O \leftrightarrow CO + 2.15H_2 \quad \Delta H_{298}^0 \approx 0 \ kJ/mol \quad (4)$$

Among these, partial oxidation of methane (POM) produces syngas with a stoichiometric H_2/CO ratio of 2.0, making it an optimum reaction for gas-to-liquids (GTL) process.

As cited by the IEA[4], global consumption of hydrogen is approximately 7.2 exajoules (EJ) annually. Hydrogen can be produced from syngas by water-gas-shift (WGS) reaction with CO_2 separation, but the downstream reactors increase the cost and complexity. Besides, the impurities from syngas, i.e., sulfur and CO are poisonous for applications such as proton-exchange membrane (PEM) fuel cell.

Here we propose a process that produces separated streams of H_2 and syngas (H_2/CO = 2) simultaneously in a single oxygen permeable membrane reactor via water splitting and POM, respectively. A schematic graph is shown in Figure 1. On the feed side, water reacts with oxygen vacancies to produce hydrogen, while oxygen incorporates into the lattice. Lattice oxygen diffuses to the sweep side where it reacts with fuels or is swept away as oxygen molecules. Thus, water dissociation on the feed side is no longer limited by thermodynamic equilibrium as O_2 is removed. Besides, the permeation of oxygen ions (lattice oxygen) to the sweep side can be optimized to suppress carbon formation during hydrocarbon fuel reforming. As methanol is among the top five large-volume products that dominate the global energy use in the chemical industry[2], the optimum H_2/CO ratio from the sweep side can benefit the GTL process. Additionally, when the heat source is solar energy, this co-production technology can be used as renewable energy storage.

This membrane approach is different from chemical looping or redox cycles for hydrogen/syngas production. In redox cycles, water and methane react with an oxygen carrier (i.e. Fe_2O_3[5,6], CeO_2[7,8] and $La_{0.8}Sr_{0.2}FeO_{3-\delta}$[9]) cyclically to produce hydrogen and syngas separately in a fluidized bed[6] or a rotary reactor[10]. An oxygen permeable membrane reactor combines the cyclical oxidization and reduction processes into one single unit. Both technologies are still under development.

Several high performance oxygen permeable materials have been proposed for water thermolysis, such as single phase perovskites, $BaCo_xFe_yZr_{1-x-y}O_{3-\delta}$ (BCFZ)[11,12], $La_{0.3}Sr_{0.7}FeO_3$[13], $La_{0.6}Sr_{0.4}Co_{0.2}Fe_{0.8}O_{3-\delta}$[14] and $La_{0.7}Sr_{0.3}Cu_{0.2}Fe_{0.8}O_{3-\delta}$[15], mixed fluorites-metal, CeO_2-Gd[16] and $Ce_{0.8}Gd_{0.2}O_{1.9-\delta}$-Cu[17] and other oxides, $SrFeCo_{0.5}O_x$[18]. At

intermediate and higher temperatures, these are all mixed ionic-electronic conductive materials. When methane is used as a sweep gas, the highest reported hydrogen production rate from water thermolysis is 3.4 μmol/cm^2•s on a BCFZ membrane with 75 vol% water-feed and 10 vol% methane-sweep at 950^{o}C[12]. A summary of the literature on co-production in an oxygen permeable membrane reactor is shown in Table 1. However, high performance Ba and Co containing perovskites often suffers from degradation such as carbonate formation or cobalt segregation, respectively[19]. Phase segregation[14], pores[20] as well as surface morphology changes[21] have also been observed during water thermolysis.

Much is yet to be learned regarding the oxygen transport process and the rate limiting steps, especially in case of co-production of H_2 and syngas. In this work, we use $La_{0.9}Ca_{0.1}FeO_{3-\delta}$ (LCF-91) membranes to examine these processes. These membranes exhibit high stability in a reducing environment as well as in the presence of water[21-24]. We show that LCF-91 membranes can be applied to co-produce H_2 and syngas (H_2/CO = 2) from water thermolysis and POM, respectively, at temperatures around 990^{o}C. A permeation model that accounts for simplified single-step chemistry on both surfaces and diffusion through the material is applied to identify the rate limiting step(s) associated with hydrogen production and oxygen permeation. Surface modification such as adding a porous layer and nickel catalysts are applied to overcome these steps as well as to increase the selectivity of syngas produced from methane oxidation. Experimental results show that surface modification on the sweep side can enhance water thermolysis on the feed side by two orders of magnitude, and syngas with H_2/CO = 2 is produced with negligible solid carbon leaving the reactor.

Water splitting on a flat membrane

Hydrogen production from water thermolysis

The test rig used in this work is a button-cell membrane reactor with an axisymmetric flow field (shown in Figure S.1). Membranes with an effective diameter 12.7 mm are tested and their dimensions are summarized in Table 2. Quartz capillary probes with 0.53 mm OD are inserted into the sweep side of the reactor to sample the local species near the membrane surface. The operating conditions are shown in Table 3. Different carrier gases for water and methane on the feed and sweep sides, respectively, are used so that the leakage around the membrane can be monitored during the experiments. Leakage into the reactor was less than 0.05% and that around the membrane was less than 0.03%. The error bars associated with the experimental results account for errors from the leakage and instrumentation uncertainties. More details regarding the setup can be found in the supplementary materials.

Previous studies showed that water thermolysis rates, compared to the homogeneous gas phase water dissociation, were enhanced when using a 0.9-mm thick flat symmetric LCF-91 membrane with inert gas sweep[21]. This is due to the heterogeneous reactions on the perovskite surface and the continuous separation of oxygen. Further enhancement of the water thermolysis rate requires a larger driving potential for oxygen transport, which can be achieved by adding fuel to the sweep gas[21]. In this work, we aim to co-produce hydrogen and syngas, and hence methane is added to the sweep gas. The experiments were carried out on the same 0.9-mm thick symmetric

membrane at 990 and 1030^{o}C. The dimensions of this membrane are shown in Table 2 as "original membrane".

Figure 2 shows results with 1 - 5 vol% methane on the sweep side. As the inlet methane concentration is raised, the hydrogen production rate on the feed side increases slowly. Yet we note that the hydrogen production rate with methane on the sweep side is two orders of magnitude lower than that observed in the case with hydrogen sweep under the same fuel concentrations which was shown in our previous study[21]. Clearly, hydrogen is more reactive on the sweep side surface than methane. Additionally, when the total sweep flow rate is raised from 100 to 500 sccm at 990^{o}C, the membrane performance doesn't change, as is shown in Figure 2.

At 1030^{o}C, hydrogen production rates from water decrease slightly at higher methane concentrations, but remains within the error bar. This can be a result of coking as reported in literature[25]. Given the low oxygen flux, carbon formed by methane decomposition on the membrane surface may not be oxidized and instead accumulates on the surface. Solid carbon covers the active membrane surface and decreases the surface reaction rate and hence, the oxygen flux. Further evidence and discussion on coking and carbon balance will be presented in the next sections.

Oxygen permeation model

A simplified model that describes the oxygen permeation flux in terms of the operating conditions and water and fuel concentrations on the feed and sweep sides, respectively, is adopted to examine the process in some detail and guide the development of more active membranes. Similar models have used before to describe oxygen

permeation with air on the feed side[26-29]. In this study, H_2O is the oxygen source and CH_4 is the sweep gas, and we modify the models accordingly. On the feed side, we develop the expression using a one-step reaction as follows:

$$H_2O + V_O^{\bullet\bullet} \underset{k_{r,H}}{\overset{k_{f,H}}{\rightleftarrows}} O_O^x + 2h^{\bullet} + H_2 . \qquad (5)$$

Here Kröger–Vink notation is used. $V_O^{\bullet\bullet}$ is the lattice oxygen vacancy, O_O^x is the lattice oxygen, $h^{\bullet}$ is the electron hole, or more precisely the net charge in the lattice iron. $k_{f,H}$ and $k_{r,H}$ are the reaction rate constants for the forward (i.e. water thermolysis) and reverse directions (i.e. hydrogen oxidation), respectively, in reaction (5).

On the sweep side, mostly partial oxidation of methane takes place as is shown in the experimental results. A one step reaction is also used to describe the surface reaction as follows:

$$O_O^x + 2h^{\bullet} + CH_4 \underset{k_{r,M}}{\overset{k_{f,M}}{\rightleftarrows}} CO + 2H_2 + V_O^{\bullet\bullet} \qquad (6)$$

where the forward and backward reaction rate constants are $k_{f,M}$ and $k_{r,M}$, respectively.

Several assumptions have been made to derive the following permeation model:

(1) The backwards reactions for both (5) and (6) are neglected due to the low hydrogen production rate and hence its low concentration compared to the species concentrations in the bulk. Similar assumptions have been made and verified in the literature for heterogeneous reactions with MIEC membranes[30];

(2) Electron hole concentrations across the membrane are assumed to be constant as the electronic transference number is much higher than ionic transference number[31,32];

(3) The oxygen site concentration inside the stoichiometric LCF-91 lattice equals to the sum of lattice oxygen and oxygen vacancy concentrations

$$C_O = C_{O_O^x} + C_V , \quad (7)$$

where C_O, $C_{O_O^x}$ and C_V are the concentrations of oxygen sites, lattice oxygen and oxygen vacancies, respectively. These concentrations are all functions of temperature and the oxygen partial pressure. The total oxygen site concentration is assumed to be constant as 0.0825 mol/cm^3 [2]estimated from XRD measurements of stoichiometric LCF-91 lattice size in air[33].

(4) The oxygen vacancy diffusion across a dense mixed ionic-electronic material follows Fick's law[19].

Validation of the assumptions and the derivation detail are shown in the supplementary material. Based on these assumptions, the vacancy flux equation can be expressed in the form of a potential difference across the membrane divided by the sum of resistances as follows:

$$J_V = \frac{C_O}{\frac{1}{k_{f,H} C'_{H_2O}} + \frac{t}{D_V} + \frac{1}{k_{f,M} C''_{CH_4}}} = \frac{\Delta P}{R_f + R_b + R_s} , \quad (8)$$

where t is the thickness of the membrane, D_V is the effective diffusivity of oxygen vacancy, C'_{H_2O} is the water concentration on the feed side and C''_{CH_4} is the methane concentration on the sweep side. ΔP is the potential difference, and R_f, R_b and R_s are the resistances of surface reaction on the feed side, the bulk diffusion and the surface reaction on the sweep side, respectively. While more elaborate models have been developed

[2] From the literature, the molar volume of stoichiometric LCF-91 is 36.37 cm^3/mol in air. As the stoichiometric number of oxygen sites is 3, the molar concentration of total oxygen sites is 0.0825 mol/cm^3.

recently[34], Equation (8) is sufficient to examine qualitatively the role of the different processes in the flux.

The effective oxygen vacancy diffusivity was derived from separate transient dilatometry studies[35], and the water thermolysis reaction rate constant was fitted in a previous study[21]. The methane oxidation reaction rate constant is fitted in this work. All the parameters needed to derive the vacancy flux at 990^{o}C are listed in Table 4. Plotting the resistance against methane concentration (Figure S.2 (b)), we can identify the rate limiting step for the oxygen flux as the surface reaction on the sweep side. It results in the highest resistance when methane concentration is 1 – 5 vol%, decreasing slowly as methane concentration rises but remaining the largest. Therefore, we conclude that attempts to enhance the performance should focus on speeding up the effective kinetics of methane partial oxidation.

Adding a porous layer for performance enhancement

Hydrogen production from water thermolysis

Methods to improve fuel-surface reactivity such as adding a porous layer and catalysts, i.e. Pt and/or CeO_2 on the sweep side, and oxygen reduction reactive layer on the feed side such as $La_{0.8}Sr_{0.2}FeO_3$ (LSF) (when air is used to oxidize the surface) have been found to enhance the oxygen flux through an LCF-91 membrane when CO is used as the sweep gas[36]. In this study, we focus on the sweep side given that the reaction on that side is the limiting step as is shown in Figure S.2. First, we increase the effective sweep side surface area by attaching a porous LCF-91 layer onto that side. The dimensions of this membrane are shown in Table 2 as “modified membrane 1”.

Results for this new configuration are shown in Figure 3. The zoom-in figure at the top left shows the hydrogen production rate from water thermolysis in the corresponding inert sweep case is 6.3×10^{-4} μmol/cm^2•s, which is in the same order of magnitude as that for the 0.9-mm symmetric membrane under the same operating conditions (shown in Figure 2). With the addition of 1 vol% methane, the hydrogen production rate from water thermolysis increases by two orders of magnitude to 0.077 μmol/cm^2•s. Further increase of the inlet methane concentration leads to higher hydrogen production until a plateau of 0.15 μmol/cm^2•s is reached at around 2 - 3 vol%.

The significant enhancement gained by attaching the porous layer is due to the increase of the surface area available for the POM reactions. Since LCF-91 is a mixed ionic-electronic conductive material, the porous layer provides an extended surface for the reaction between methane and lattice oxygen, and hence reduces the corresponding resistance. This is similar to what is observed in the triple phase boundary in the electrodes of a solid oxide fuel cell[37].

As shown in Figure 3, the performance reaches a plateau at methane concentrations of 2 – 3 vol%. This could be due to carbon formation and deposition on the surface at higher methane concentration, which covers the active surface of the porous layer. This hypothesis is supported by the carbon balance depicted in Figure 4. The carbon balance is defined as the ratio of the carbon content of the gaseous species at the reactor outlet over that at the inlet. It is less than unity especially at methane concentration greater than 3 vol%, which indicates the existence of solid carbon species. Following the experiments, carbon black was also found inside the reactor.

Thermodynamic equilibrium calculation using Cantera[38] with GRI-Mech 3.0 mechanism[39] shows that homogeneous methane pyrolysis in the gas phase at 990^{o}C produces primarily H_2, C_2H_2 and C_2H_4, with carbon molar fraction as low as 3.5×10^{-19}. Therefore, we suggest that carbon on the membrane surface is formed via heterogeneous methane decomposition, while the oxidation of carbon is slow because of the small amount of lattice oxygen available on the sweep side. Similar carbon formation has been reported on reduced metal catalysts such as Co, Ni and Fe during catalytic methane decomposition at elevated temperatures[40].

The H_2/CO ratio at the outlet on the sweep side is shown in Figure 4. For all concentrations, the H_2/CO ratio is around 2.7, which is higher than the ratio expected in the stoichiometric POM reactions. Meanwhile, very low CO_2 concentrations, around 0.001%, are detected at the outlet of the sweep side. These indicate that excessive amount of hydrogen was produced via heterogeneous methane decomposition, with only a fraction of the carbon getting oxidized to CO and CO_2 and the rest remaining in the solid carbon form, supporting again the lack of suffice oxygen on the sweep side.

Methane decomposition and carbon oxidation

In our experiments, coke, CO and CO_2 are all observed near the membrane surface at finite concentrations, indicating that the three end states of methane surface reaction shown in Figure 5 could occur simultaneously: (a) decomposition into carbon and hydrogen; (b) partial oxidation of carbon; or (c) full oxidation of carbon. Decomposition on a reduced surface results in coking, which has been observed on $LaNi_{1-x}M_xO_{3-\delta}$ (M = Co and Fe) catalysts[41] and on a LCF-91 membrane[42]. If not oxidized,

carbon remains attached to an otherwise active site and slows down the surface reaction in a manner similar to catalyst poisoning[43]. On the other hand, carbon oxidation can follow either partial oxidation or combustion depending on catalysts and reactant flow rates[44]. As lattice oxygen is more active than gas-phase oxygen species in oxidizing carbon species[45], the oxygen flux from water thermolysis on the feed side can affect the relative concentrations of these carbon species.

As discussed in the previous section, the surface reaction on the sweep side is the limiting step. Carbon covering the surface active sites (pathway (a)) is related to the drop of the oxygen flux at high methane concentrations at higher temperature i.e. 1030 ^{o}C (Figure 2) and the leveling off in hydrogen production rate from water beyond 3 vol% of methane (Figure 3). Similar results have been reported for catalytic decomposition of methane, that higher operating temperature and methane concentration lead to faster catalysts deactivation due to encapsulation of active catalytic sites by deposited carbon[46]. Therefore, in order to further enhance the flux, we need to provide more active sites on the sweep side, or enhance carbon oxidation rates and thus prevent it from blocking these sites.

Further enhancements using a nickel catalyst

Hydrogen production from water thermolysis

In order to increase the oxygen flux further, we added a catalyst to the porous layer on the sweep side to accelerate the surface reaction. Nickel catalysts are reported to be one of the most effective base metal catalysts for POM in both packed bed or membrane reactors[44,47,48]. While solid carbon is prone to form on nickel from methane

decomposition, it is found that the active lattice oxygen from the catalysts or the support can facilitate the oxidation of surface carbon[47] or soot[49,50]. In this work, nickel is applied onto the porous LCF-91 layer by wet impregnation. Because LCF-91 is a good oxygen conductor, the synergic effect between the porous LCF-91 support and the nickel catalysts is expected to improve the performance.

We examined the elemental distribution of the porous layer by EDX to identify nickel after wet impregnation (Figure S.4). The concentration of nickel particles in porous layer is 0.4 wt%, which was found by weighing the membrane before and after impregnation. The dimension of this membrane is shown in Table 2 under "modified membrane 2".

The hydrogen production rate from water thermolysis is shown in Figure 6. It continues to rise with increasing methane concentration, reaching more than double the value without a catalyst ("modified membrane 1" in Figure 3). Given that the LCF-91 porous layer for both membranes are the same and that the bulk diffusion is not the limiting step with 1-5 vol% methane sweep, the thickness of the dense membrane is not expected to affect the results significantly and the enhancement of the oxygen flux is attributed to the increase of reaction rate on the sweep surface by the nickel catalysts. Besides, the hydrogen production rate from water continues to increase slowly with increasing methane concentration, as adding nickel reduces the fraction of carbon attached to the surface by raising the oxygen flux. However, further studies are needed to examine the details of the suggested enhancement mechanism.

Syngas production

As is shown in Figure 7, the CH_4/O_2 ratio increases from 3.3 to 11.0 when the inlet methane concentration is raised from 1 to 5 vol%; this shows a slower rise in the oxygen flux as methane concentration increases. This also leads to lower methane conversions at higher inlet methane concentrations: conversion rate is almost 80% when the inlet methane concentration is 1 vol%, but it drops to around 20% at 5 vol% methane.

The products at the reactor outlet are shown in Figure 8. Syngas with H_2/CO ratio of 2 is measured in all cases with 1-5 vol% inlet methane concentrations. This matches well with the stoichiometric ratio in POM reaction. Besides, the H_2/CO ratio stays constant when CH_4 inlet concentration increases. Thus, CH_4/O_2 ratio doesn't affect the syngas selectivity on this surface modified oxygen permeable membrane. Furthermore, in Figure 8 (b), plots of hydrogen productions versus methane consumptions fall well on the 2:1 line in all cases. These indicate that syngas is produced by a combined effect of surface and gas phase reactions on the sweep side.

There are three different end states for methane reaction as illustrated before in Figure 5. The carbon balance in the gas phase in Figure 9 shows that the gaseous carbon species near the membrane surface and at the outlet of the sweep side match very well with those at the inlet. As almost all the carbon species are in the gas phase, this means that the solid carbon deposition pathway is very unlikely in this LCF-91 porous layer with nickel catalysts under the operating conditions in our experiments. Compared with the observed carbon formation without nickel catalysts (in Figure 4), the higher oxygen fluxes and the enhancement of surface reaction by nickel are attributed to less solid carbon, as is observed in Figure 9.

The selectivity to CO_2 is defined as

$$S_{CO_2} = \frac{n''_{CO_2,out}}{n''_{CO,out} + n''_{CO_2,out}} \qquad (9)$$

where n'' is the molar flow rate of the species on the sweep side, mol/s. This value illustrates the relative importance of the full oxidation pathway. Figure 10 shows that S_{CO_2} close to the membrane surface is around 8% when the inlet methane concentration is 1 vol%, and decreases to 0.55% at 5 vol% methane. Full oxidation is less favorable at higher CH_4:O_2 ratio, as less oxygen is available to fully oxidize the carbon species. Yet S_{CO_2} at the outlet is always lower than its value near the surface, showing that CO_2 generated by full oxidation on the membrane surface reforms methane to produce CO when the products travel from the surface to the reactor exit.

Previous studies on packed catalytic bed reactors showed that methane tends to be oxidized into CO_2 and H_2O on nickel surface; therefore, it is proposed that syngas is formed in the gas phase by dry or steam reforming[51]. However, in our case, the available oxygen depends on the water thermolysis reaction on the feed side. Therefore, whether the adsorbed carbon species are oxidized into CO or CO_2 depends on the oxygen flux or the water thermolysis rate.

Conclusions and future work

LCF-91 exhibits good ionic and electronic conductivities at elevated temperatures. Studies have shown the application of LCF-91 membrane for oxygen production, oxy-fuel combustion and syngas production. In this paper, we investigate the co-production of

H_2 and syngas on LCF-91 membranes and demonstrate that the understanding of the transport phenomenon guides better membrane and reactor designs.

Original symmetric membranes and two surface modified asymmetric membranes were tested, with the latter accomplished by adding a porous layer and nickel catalysts to improve performance. Results show the following:

(1) For water thermolysis and POM on a 0.9-mm thick flat LCF-91 membrane, the permeation model shows that the limiting step is the surface reaction on the sweep side. Higher temperature leads to higher water thermolysis rates, while the concentration of methane on the sweep side has small effect on that rate.

(2) Performance is improved by applying a 0.4-mm thick porous LCF-91 layer on a 0.5-mm thick dense LCF-91 membrane. The hydrogen production rate from water thermolysis increases by two orders of magnitude compared to the original membrane. However, due to the lack of sufficient oxygen on the sweep side, carbon formation from methane decomposition is observed and the H_2/CO ratios of the syngas produced on the sweep side are around 2.7.

(3) Nickel catalyst is applied on the porous LCF-91 layer to further improve the performances. The hydrogen production rate from water thermolysis further increases by a factor of 2 with the maximum value reaching 0.37 $\mu mol/cm^2 \cdot s$ at 990^oC. Syngas produced on the sweep side has a H_2/CO ratio of 2 when the inlet methane concentration changes from 1 to 5 vol%. This is due to the combined effect of reactions on the surface and in the gas phase. Besides, hardly any solid carbon is found from carbon balance in gas species.

(4) Under different conditions, finite amount of coke, CO and CO_2 are observed near the membrane surface. The oxygen fluxes and CH_4/O_2 ratios affect the relative concentration of these carbon species.

Further studies of the synergic effects between LCF-91 and Ni on POM in a membrane reactor are needed, especially when using thinner membranes and optimum porous support thickness. Besides, further examination of the surface reaction mechanism which affects the oxygen flux through the membrane is also important for designing better membranes and catalysts. The complexity of the combined effects of the reactions on the solid surface and in the gas phase as well as the flow fields in the porous layer and membrane reactor also requires more investigations from both experimental and numerical aspects to understand the co-production process.

Acknowledgement

The authors would like to thank both Shell and the King Abdullah University of Science and Technology (KAUST) for funding the research. This contribution was identified by Dr. Dushyant Shekhawat (National Energy Technology Laboratory) as the Best Presentation in the session "Fuel Processing for Hydrogen Production" of the 2015 AIChE Annual Meeting in Salt Lake City.

Literature Cited

1. Nguyen VN, Blum L. Syngas and Synfuels from H_2O and CO_2: Current Status. *Chem. Ing. Tech.* 2015;87(4):354-375.

2. Rightor EG, Tway CL. Global energy & emissions reduction potential of chemical process improvements. *Catal. Today.* 2015;258, Part 2:226-229.

3. NETL. Syngas optimized for intended products. 2015; http://www.netl.doe.gov/research/coal/energy-systems/gasification/gasifipedia/syngas-optimization.

4. IEA. Technology Roadmap: hydrogen and fuel cells 2015.

5. Luo S, Zeng L, Xu D, et al. Shale gas-to-syngas chemical looping process for stable shale gas conversion to high purity syngas with a H_2 : CO ratio of 2 : 1. *Energy Environ. Sci.* 2014;7(12):4104-4117.

6. Deshpande N, Majumder A, Qin L, Fan LS. High-Pressure Redox Behavior of Iron-Oxide-Based Oxygen Carriers for Syngas Generation from Methane. *Energy & Fuels.* 2015;29(3):1469-1478.

7. Furler P, Scheffe JR, Steinfeld A. Syngas production by simultaneous splitting of H_2O and CO_2 via ceria redox reactions in a high-temperature solar reactor. *Energy Environ. Sci.* 2012;5(3):6098-6103.

8. Hao Y, Yang C-K, Haile SM. High-temperature isothermal chemical cycling for solar-driven fuel production. *PCCP.* 2013;15(40):17084-17092.

9. He F, Li F. Perovskite promoted iron oxide for hybrid water-splitting and syngas generation with exceptional conversion. *Energy Environ. Sci.* 2015;8(2):535-539.

10. Zhao Z, Iloeje CO, Chen T, Ghoniem AF. Design of a rotary reactor for chemical-looping combustion. Part 1: Fundamentals and design methodology. *Fuel.* 2014;121:327-343.

11. Jiang H, Cao Z, Schirrmeister S, Schiestel T, Caro J. A Coupling Strategy to Produce Hydrogen and Ethylene in a Membrane Reactor. *Angew. Chem. Int. Ed.* 2010;49(33):5656-5660.

12. Jiang H, Wang H, Werth S, Schiestel T, Caro J. Simultaneous Production of Hydrogen and Synthesis Gas by Combining Water Splitting with Partial Oxidation of Methane in a Hollow-Fiber Membrane Reactor. *Angew. Chem. Int. Ed.* 2008;47(48):9341-9344.

13. Nalbandian L, Evdou A, Zaspalis V. $La_{1-x}Sr_xMO_3$ (M = Mn, Fe) perovskites as materials for thermochemical hydrogen production in conventional and membrane reactors. *Int. J. Hydrogen Energy.* 2009;34(17):7162-7172.

14. Franca RV, Thursfield A, Metcalfe IS. $La_{0.6}Sr_{0.4}Co_{0.2}Fe_{0.8}O_{3-\delta}$ microtubular membranes for hydrogen production from water splitting. *J. Membr. Sci.* 2012;389(0):173-181.

15. Park CY, Lee TH, Dorris SE, Balachandran U. Hydrogen production from fossil and renewable sources using an oxygen transport membrane. *Int. J. Hydrogen Energy.* 2010;35(9):4103-4110.

16. Balachandran U, Lee T, Dorris S. Hydrogen production by water dissociation using mixed conducting dense ceramic membranes. *Int. J. Hydrogen Energy.* 2007;32(4):451-456.

17. Song SJ, Moon JH, Ryu HW, Lee TH, Dorris SE, Balachandran U. Non-galvanic hydrogen production by water splitting using cermet membranes. *J. Ceramic Process. Res.* 2008;9(2):123-125.

18. Lee TH, Park CY, Dorris SE, Balachandran U. Hydrogen Production by Steam Dissociation using Oxygen Transport Membranes. *ECS Trans.* 2008;13(26):379-384.

19. Sunarso J, Baumann S, Serra JM, et al. Mixed ionic–electronic conducting (MIEC) ceramic-based membranes for oxygen separation. *J. Membr. Sci.* 2008;320(1-2):13-41.

20. Park CY, Lee TH, Dorris SE, Lu Y, Balachandran U. Oxygen permeation and coal-gas-assisted hydrogen production using oxygen transport membranes. *Int. J. Hydrogen Energy.* 2011;36(15):9345-9354.

21. Wu XY, Chang L, Uddi M, Kirchen P, Ghoniem AF. Toward enhanced hydrogen generation from water using oxygen permeating LCF membranes. *PCCP.* 2015;17(15):10093-10107.

22. Hunt A, Dimitrakopoulos G, Ghoniem AF. Surface oxygen vacancy and oxygen permeation flux limits of perovskite ion transport membranes. *J. Membr. Sci.* 2015;489:248-257.

23. Polfus JM, Xing W, Pećanac G, et al. Oxygen permeation and creep behavior of $Ca_{1-x}Sr_xTi_{0.6}Fe_{0.15}Mn_{0.25}O_{3-\delta}$ (x=0, 0.5) membrane materials. *J. Membr. Sci.* 2016;499:172-178.

24. Anderson LL, Armstrong PA, Broekhuis RR, et al. Advances in ion transport membrane technology for oxygen and syngas production. *Solid State Ionics.* 2016;*288*:331-337.

25. Michalsky R, Neuhaus D, Steinfeld A. Carbon Dioxide Reforming of Methane using an Isothermal Redox Membrane Reactor. *Energy Technology.* 2015;3(7):784-789.

26. Hong J, Kirchen P, Ghoniem AF. Numerical simulation of ion transport membrane reactors: Oxygen permeation and transport and fuel conversion. *J. Membr. Sci.* 2012;407-408:71-85.

27. Xu SJ, Thomson WJ. Oxygen permeation rates through ion-conducting perovskite membranes. *Chem. Eng. Sci.* 1999;54(17):3839-3850.

28. Wang Z, Yang N, Meng B, Tan X, Li K. Preparation and Oxygen Permeation Properties of Highly Asymmetric $La_{0.6}Sr_{0.4}Co_{0.2}Fe_{0.8}O_{3-\delta}$ Perovskite Hollow-Fiber Membranes. *Ind. Eng. Chem. Res.* 2008;48(1):510-516.

29. ten Elshof JE, Bouwmeester HJM, Verweij H. Oxygen transport through $La_{1-x}Sr_xFeO_{3-\delta}$ membranes. I. Permeation in air/He gradients. *Solid State Ionics.* 1995;81(1–2):97-109.

30. Hong J, Kirchen P, Ghoniem AF. Analysis of heterogeneous oxygen exchange and fuel oxidation on the catalytic surface of perovskite membranes. *J. Membr. Sci.* 2013;445:96-106.

31. Bidrawn F, Lee S, Vohs JM, Gorte RJ. The Effect of Ca, Sr, and Ba Doping on the Ionic Conductivity and Cathode Performance of $LaFeO_3$. *J. Electrochem. Soc.* 2008;155(7):B660-B665.

32. Hung M-H, Rao MVM, Tsai D-S. Microstructures and electrical properties of calcium substituted $LaFeO_3$ as SOFC cathode. *Mater. Chem. Phys.* 2007;101(2–3):297-302.

33. Pecchi G, Jiliberto MG, Buljan A, Delgado EJ. Relation between defects and catalytic activity of calcium doped LaFeO3 perovskite. *Solid State Ionics.* 2011;187(1):27-32.

34. Dimitrakopoulos G, Ghoniem AF. A two-step surface exchange mechanism and detailed defect transport to model oxygen permeation through the La0.9Ca0.1FeO3−δmixed-conductor. *J. Membr. Sci.* 2016;510:209-219.

35. Hunt A, Dimitrakopoulos G, Kirchen P, Ghoniem AF. Measuring the oxygen profile and permeation flux across an ion transport membrane and the development and validation of a multistep surface exchange model. *J. Membr. Sci.* 2014;468:62-72.

36. Yu AS, Kim J, Oh T-S, Kim G, Gorte RJ, Vohs JM. Decreasing interfacial losses with catalysts in $La_{0.9}Ca_{0.1}FeO_{3-\delta}$ membranes for syngas production. *Applied Catalysis A: General.* 2014;486:259-265.

37. Adler SB. Factors Governing Oxygen Reduction in Solid Oxide Fuel Cell Cathodes. *Chem. Rev.* 2004;104(10):4791-4844.

38. Goodwin DG. Cantera. http://www.aresinstitute.org/Cantera/cantera-cxx.pdf.

39. Smith GP, Golden DM, Frenklach M, et al. GRI-Mech 3.0. http://www.me.berkeley.edu/gri_mech/.

40. Ahmed S, Aitani A, Rahman F, Al-Dawood A, Al-Muhaish F. Decomposition of hydrocarbons to hydrogen and carbon. *Applied Catalysis A: General.* 2009;359(1–2):1-24.

41. Maneerung T, Hidajat K, Kawi S. Co-production of hydrogen and carbon nanofibers from catalytic decomposition of methane over $LaNi_{1-x}M_xO_{3-\alpha}$

perovskite (where M = Co, Fe and x = 0, 0.2, 0.5, 0.8, 1). *Int. J. Hydrogen Energy.* 2015;40(39):13399-13411.

42. Dimitrakopoulos G, Ghoniem AF. Role of gas-phase and surface chemistry in methane reforming using a oxygen transport membrane. *Proceedings of the Combustion Institute.* 2016;*in press*.

43. Rostrup-Nielsen J, Trimm DL. Mechanisms of carbon formation on nickel-containing catalysts. *J. Catal.* 1977;48(1):155-165.

44. Kathiraser Y, Kawi S. $La_{0.6}Sr_{0.4}Co_{0.8}Ga_{0.2}O_{3-\delta}$ (LSCG) hollow fiber membrane reactor: Partial oxidation of methane at medium temperature. *AlChE J.* 2013;59(10):3874-3885.

45. Gür TM. Comprehensive review of methane conversion in solid oxide fuel cells: Prospects for efficient electricity generation from natural gas. *Prog. Energy Combust. Sci.* 2016;54:1-64.

46. Ashik UPM, Wan Daud WMA, Abbas HF. Production of greenhouse gas free hydrogen by thermocatalytic decomposition of methane – A review. *Renewable and Sustainable Energy Reviews.* 2015;44:221-256.

47. Christian Enger B, Lødeng R, Holmen A. A review of catalytic partial oxidation of methane to synthesis gas with emphasis on reaction mechanisms over transition metal catalysts. *Applied Catalysis A: General.* 2008;346(1–2):1-27.

48. Yuan R-h, He Z, Zhang Y, et al. Partial oxidation of methane to syngas in a packed bed catalyst membrane reactor. *AlChE J.* 2016:in press.

49. Dhakad M, Rayalu SS, Kumar R, et al. Low Cost, Ceria Promoted Perovskite Type Catalysts for Diesel Soot Oxidation. *Catal. Lett.* 2008;121(1-2):137-143.

50. Xiao P, Zhong L, Zhu J, et al. CO and soot oxidation over macroporous perovskite LaFeO3. *Catal. Today.* 2015;258, Part 2:660-667.

51. York APE, Xiao TC, Green MLH. Brief overview of the partial oxidation of methane to synthesis gas. *Top. Catal.* 2003;22(3-4):345-358.

52. Jiang H, Liang F, Czuprat O, et al. Hydrogen production by water dissociation in surface-modified $BaCo_xFe_yZr_{1-x-y}O_{3-\delta}$ hollow-fiber membrane reactor with improved oxygen permeation. *Chemistry.* 2010;16(26):7898-7903.

53. Jiang H, Wang H, Liang F, et al. Improved water dissociation and nitrous oxide decomposition by in situ oxygen removal in perovskite catalytic membrane reactor. *Catal. Today.* 2010;156(3–4):187-190.

54. Balachandran U, Lee TH, Wang S, Dorris SE. Use of mixed conducting membranes to produce hydrogen by water dissociation. *Int. J. Hydrogen Energy.* 2004;29(3):291-296.

55. Szabo V, Bassir M, Van Neste A, Kaliaguine S. Perovskite-type oxides synthesized by reactive grinding: Part IV. Catalytic properties of $LaCo_{1-x}Fe_xO_3$ in methane oxidation. *Applied Catalysis B: Environmental.* 2003;43(1):81-92.

List of Table Captions

List of Figure Captions:

Figure 1 A schematic diagram showing the oxygen transport process with water thermolysis on the feed side and partial oxidation of methane (POM) on the sweep side. LCF-91 perovskite membrane is used to illustrate the process in a dense mixed ionic-electronic conductive (MIEC) membrane

Figure 2 For a 0.9-mm thick flat LCF-91 membrane, the methane (1-5 vol%) on sweep side has small enhancement effects on the hydrogen production rate from water thermolysis at elevated temperatures of 990 and 1030oC

Figure 3 By adding a porous layer on the sweep side, the hydrogen production rate from water thermolysis increases by two orders of magnitude compared to the original membrane in Figure 2. However, with increasing methane concentration on the sweep side, the hydrogen production rate reaches a plateau. The zoom-in figure shows the hydrogen production rate in helium sweep case

Figure 4 Carbon balance in the gas phase is around unity at low CH4 concentration, but less than unity at higher CH4 concentrations. The H2/CO ratios at the outlet are around 2.7, which is higher than the stoichiometric value of POM

Figure 5 Schematic diagram illustrates three possible products of methane decomposition and carbon oxidation on the sweep surface: (a) decomposition into carbon and hydrogen; (b) partial oxidation of carbon; or (c) full oxidation of carbon

Figure 6 The nickel catalysts on the porous layer further enhances the hydrogen production rates from water thermolysis to double of those values without nickel catalysts in Figure 3. Further increase of the inlet methane concentration leads to slow rise of hydrogen production rate

Figure 7 When the inlet methane concentration changes from 1 to 5 vol%, the CH4/O2 ratio rises due to the slower increase of oxygen flux at higher inlet methane concentration. The conversion ratio of methane decreases at higher inlet methane concentration

Figure 8 (a) The syngas at the outlet of the reactor has a H2/CO ratio of 2 which shows that POM reaction takes place in the sweep side chamber with a combined effort of reactions on the surface and in the gas phase (The dotted line shows a ratio of 2)

Figure 8 (b) Hydrogen atoms in methane are converted to hydrogen molecules at the outlet of the reactor (The dotted line shows a $n_{H_2} \diagup \Delta n_{CH_4}$ ratio of 2). The numbers in the brackets near the symbols represent the methane concentration at that specific data point. On both figures, the numbers in the brackets near the symbols represent the inlet methane concentration at that specific data point, and Q''_i is the flow rate of species *i* on sweep side under standard condition

Figure 9 On the sweep side, the gaseous carbon species near the local membrane surface and at the outlet both match well with the inlet carbon species, showing that hardly any solid carbon was formed. $Q"_i$ is the flow rate of species *i* on sweep side under standard condition

Figure 10 The selectivity to CO2 is higher near the local membrane surface than that at the outlet. At inlet higher methane concentration, the local CO2 selectivity decrease

Table 1 Different membranes were tested in literature for co-production of hydrogen and syngas from water thermolysis and POM, respectively

Ref	Membrane materials	Sweep side catalysts	T [^{o}C]	Products on the sweep side	Maximum H_2 production rate from water [μmol/cm^2•s]	H_2O dissociation ratio [%]
[12]	BCFZ	Ni-based	950	S_{CO} = 3 ~ 45%; Coke formation found	3.4	14.3
[52]	BCFZ	BCFZ + Pd	800 - 950	N/A	1.4	6.02
[53]	BCFZ	Ni/Al_2O_3	800 - 950	N/A	2.2	8.89
[54]	CGO*	?*	900	N/A	4.1	N/A
[14]	LSCF	/	900	S_{H2} = 36 - 77%; S_{CO2} = ~70%	0.21#	~5.6

BCFZ: $BaCo_xFe_yZr_{1-x-y}O_{3-\delta}$

CGO: Gd-doped CeO_2

LSCF: $La_{0.6}Sr_{0.4}Co_{0.2}Fe_{0.8}O_{3-\delta}$

S_i: the selectivity to product *i*

* The membrane might contain Ni as cited by the same research group in [16]

The value is based on inner tube surface area

Table 2 Summary of membrane configurations

		Original membrane	Modified membrane 1	Modified membrane 2
Thickness	Dense [mm]	0.9	0.5	0.9
	Porous [mm]	/	0.4	0.4
Effective diameter	Dense [mm]	12.70	12.70	12.70
	Porous [mm]	/	12.37	11.53
Catalysts		/	/	Nickel

Table 3 Operating conditions

Temperature [^{o}C]	Feed side			Sweep side		
	Carrier gas	H_2O concentration	Total flow rate [sccm]	Carrier gas	CH_4 concentration	Total flow rate [sccm]
990 – 1030	Argon	50 vol%	400	Helium	1 – 5 vol%	100, 500

Table 4 Reaction kinetic parameters for bulk diffusion and surface reactions at 990^{o}C for LCF-91 membrane

	Parameter	Unit	Value	Ref value
(1) Vacancy diffusivity	D_{v}	[cm^2/s]	$1.7 \times 10^{-5\ 35}$	
(2) Water thermolysis	$k_{f,\mathrm{H}}$	[cm^4/mol•s]	$1.4 \times 10^{-1\ 21}$	
(3) Methane oxidation	$k_{f,M}$	[cm^4/mol•s]	3.0×10^{-2}	$\sim 1.75 \times 10^{-1*55}$
* The reference value is for full oxidation of CH_4 and O_2 co-fed in packed catalysts of $La_{0.99}Fe_{1.01}O_{3-\delta}$ at 990^{o}C				

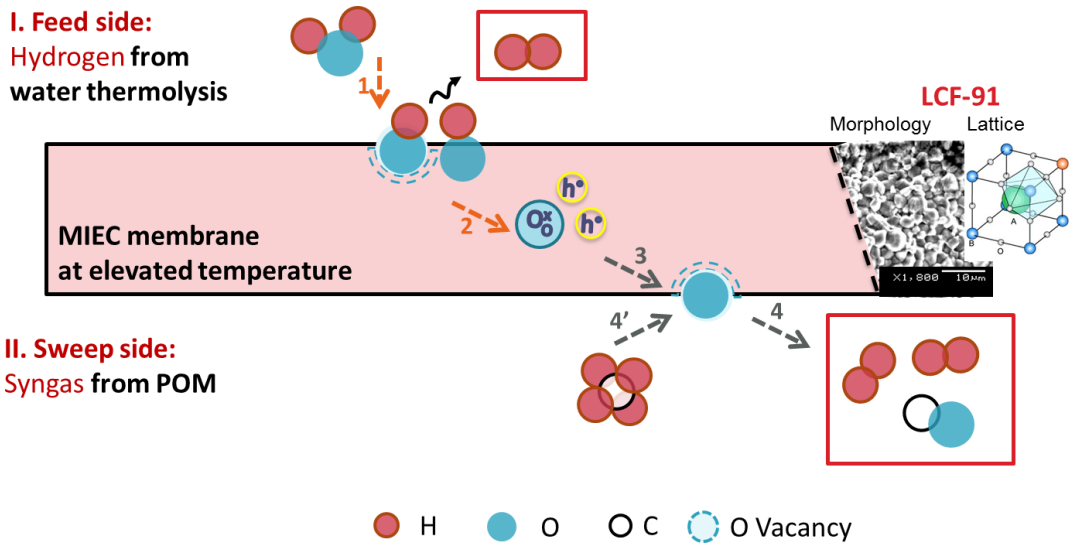

Figure 1 A schematic diagram showing the oxygen transport process with water thermolysis on the feed side and partial oxidation of methane (POM) on the sweep side. LCF-91 perovskite membrane is used to illustrate the process in a dense mixed ionic-electronic conductive (MIEC) membrane

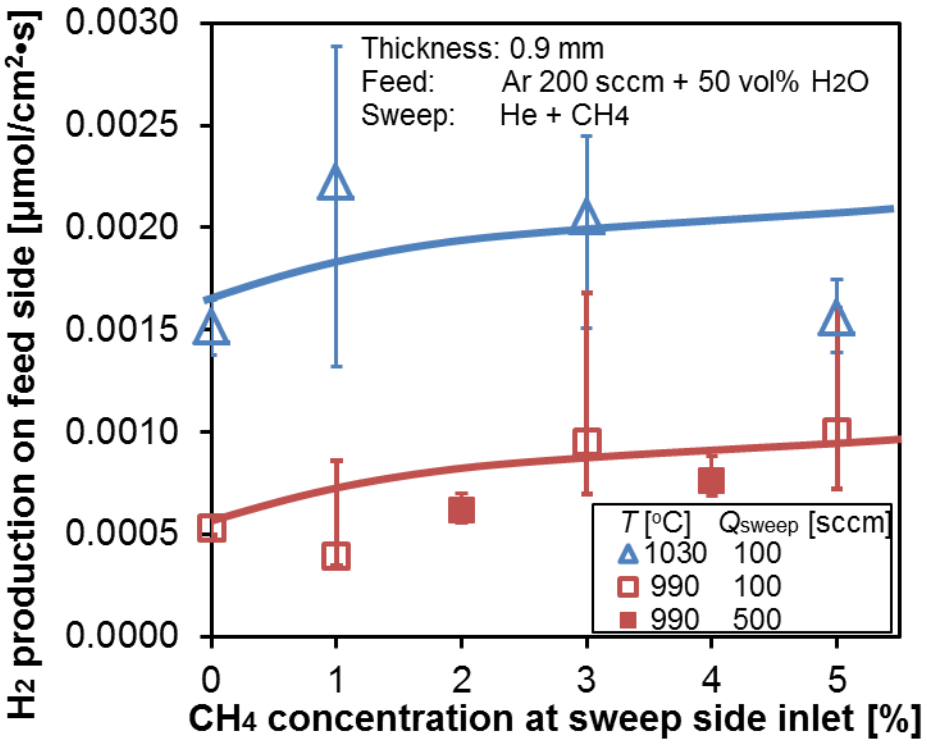

Figure 2 For a 0.9-mm thick flat LCF-91 membrane, the methane (1-5 vol%) on sweep side has small enhancement effects on the hydrogen production rate from water thermolysis at elevated temperatures of 990 and 1030^{o}C

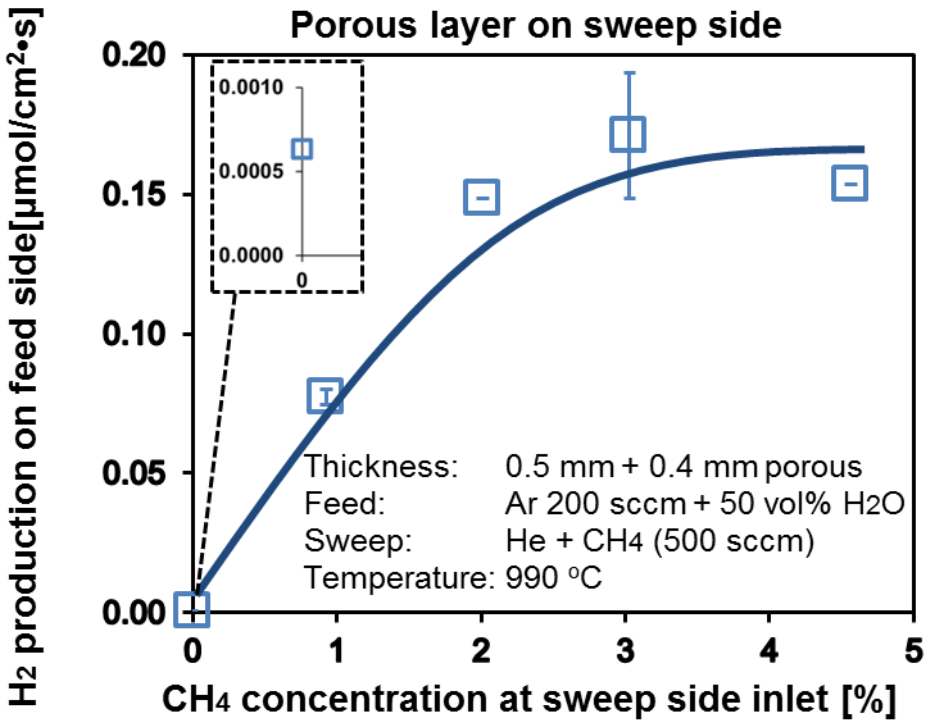

Figure 3 By adding a porous layer on the sweep side, the hydrogen production rate from water thermolysis increases by two orders of magnitude compared to the original membrane in Figure 2. However, with increasing methane concentration on the sweep side, the hydrogen production rate reaches a plateau. The zoom-in figure shows the hydrogen production rate in helium sweep case

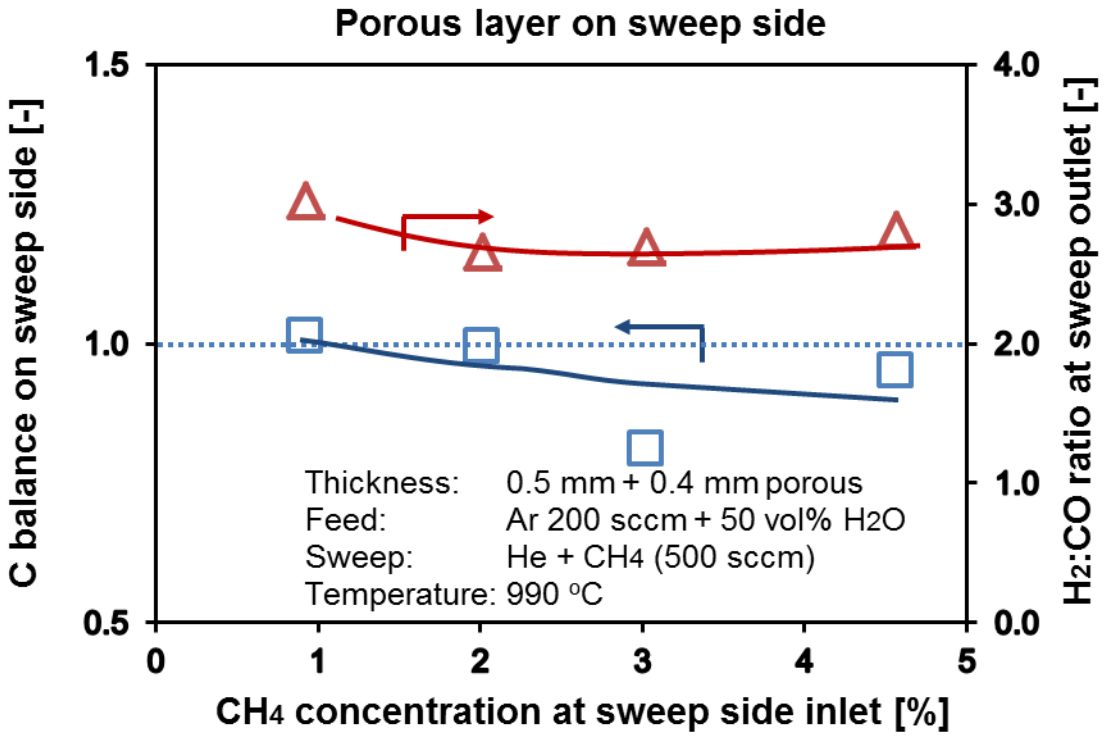

Figure 4 Carbon balance in the gas phase is around unity at low CH_4 concentration, but less than unity at higher CH_4 concentrations. The H_2/CO ratios at the outlet are around 2.7, which is higher than the stoichiometric value of POM reaction

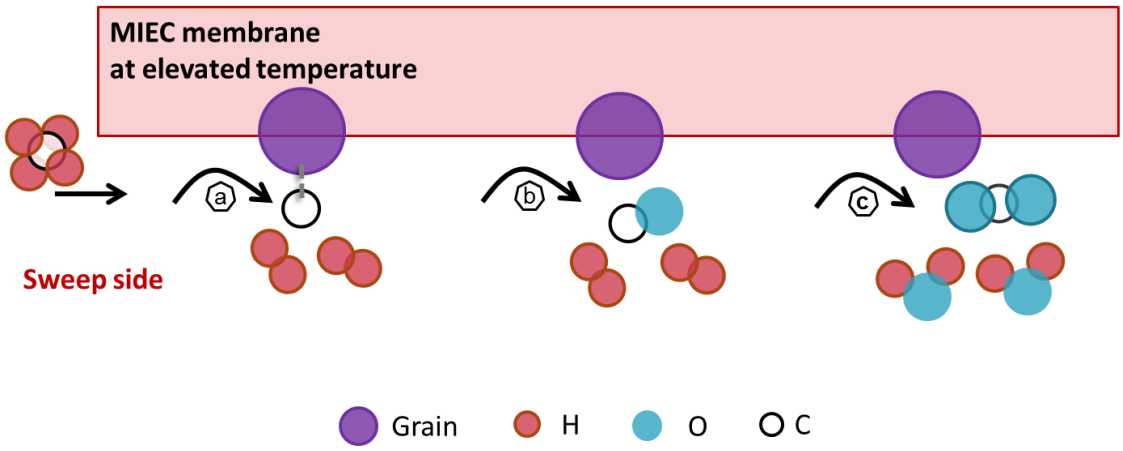

Figure 5 Schematic diagram illustrates three possible products of methane decomposition and carbon oxidation on the sweep surface: (a) decomposition into carbon and hydrogen; (b) partial oxidation of carbon; or (c) full oxidation of carbon

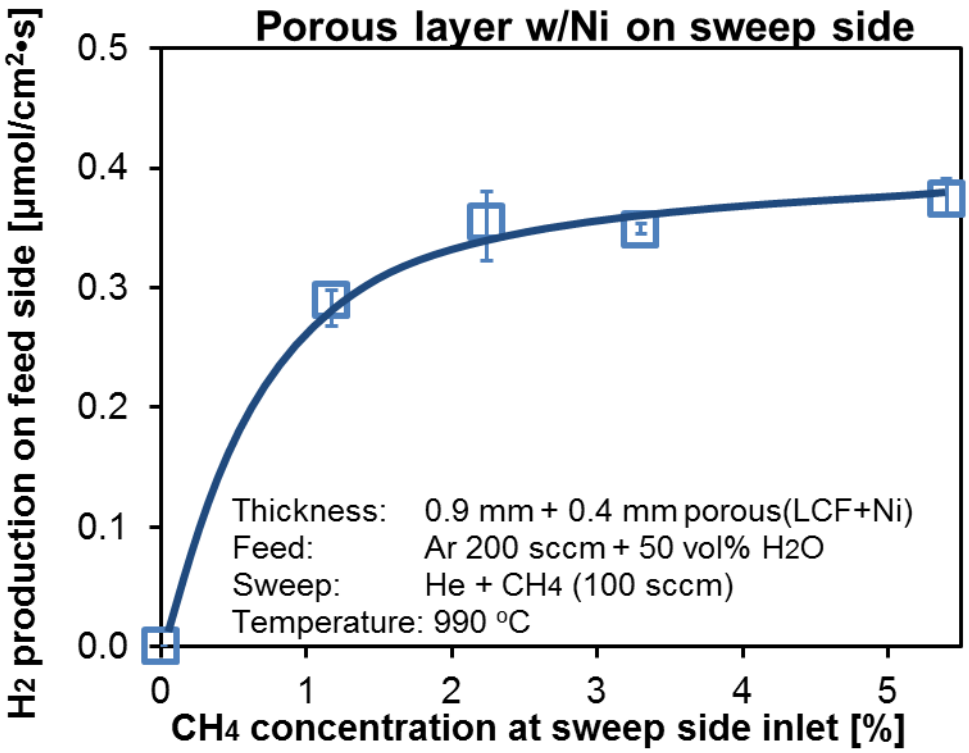

Figure 6 The nickel catalysts on the porous layer further enhances the hydrogen production rates from water thermolysis to double of those values without nickel catalysts in Figure 3. Further increase of the inlet methane concentration leads to slow rise of hydrogen production rate

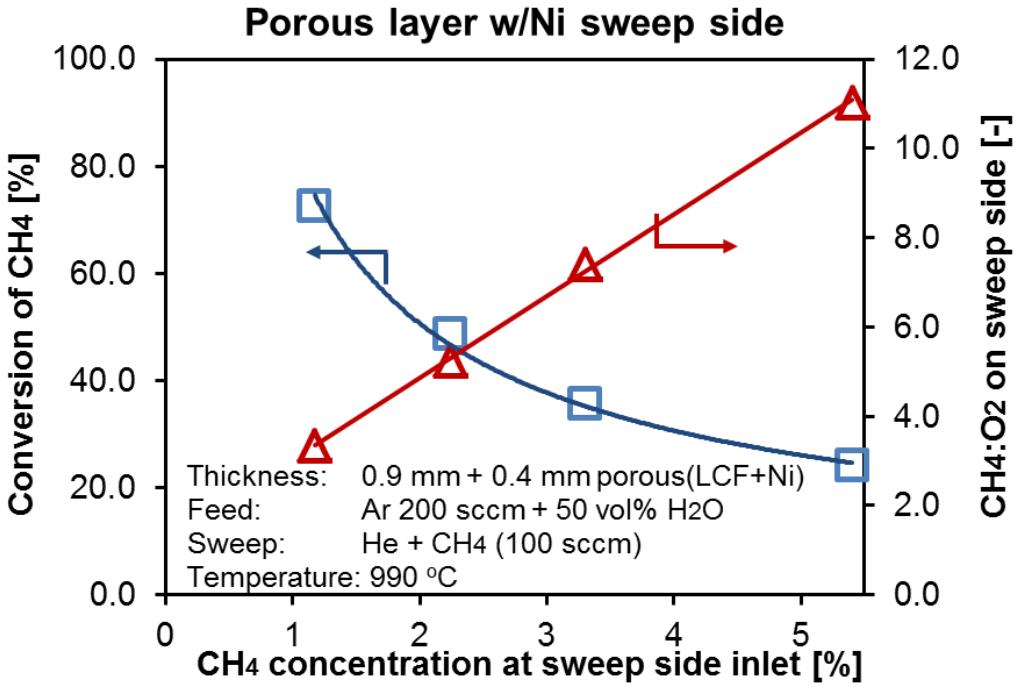

Figure 7 When the inlet methane concentration changes from 1 to 5 vol%, the CH_4/O_2 ratio rises due to the slower increase of oxygen flux at higher inlet methane concentration. The conversion ratio of methane decreases at higher inlet methane concentration

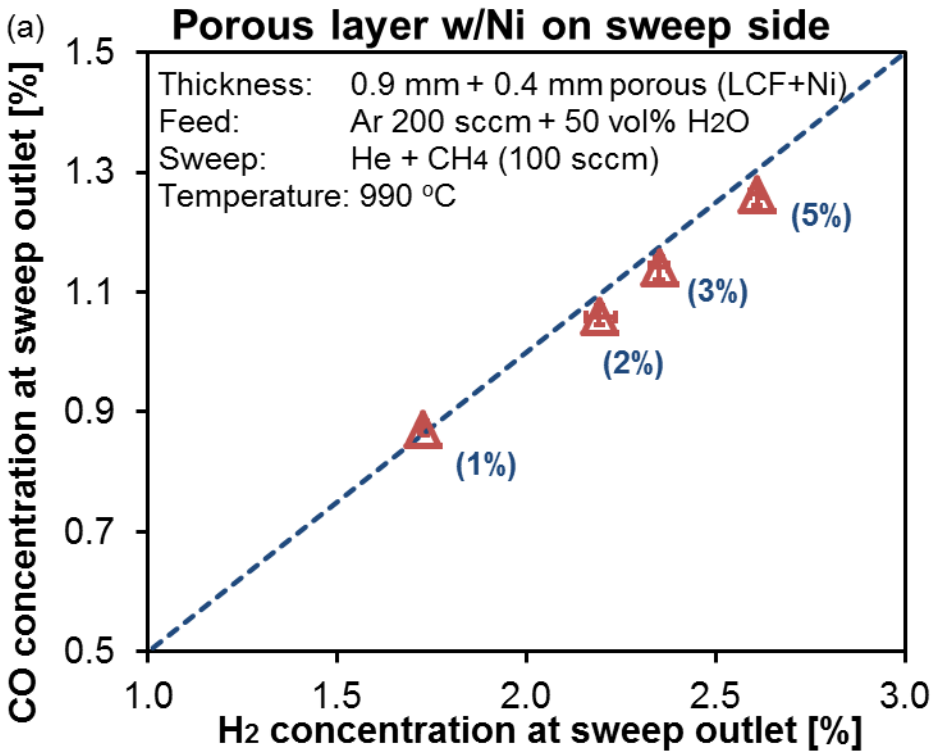

Figure 8 (a) The syngas at the outlet of the reactor has a H_2/CO ratio of 2 which shows that POM reaction takes place in the sweep side chamber with a combined effort of reactions on the surface and in the gas phase (The dotted line shows a ratio of 2)

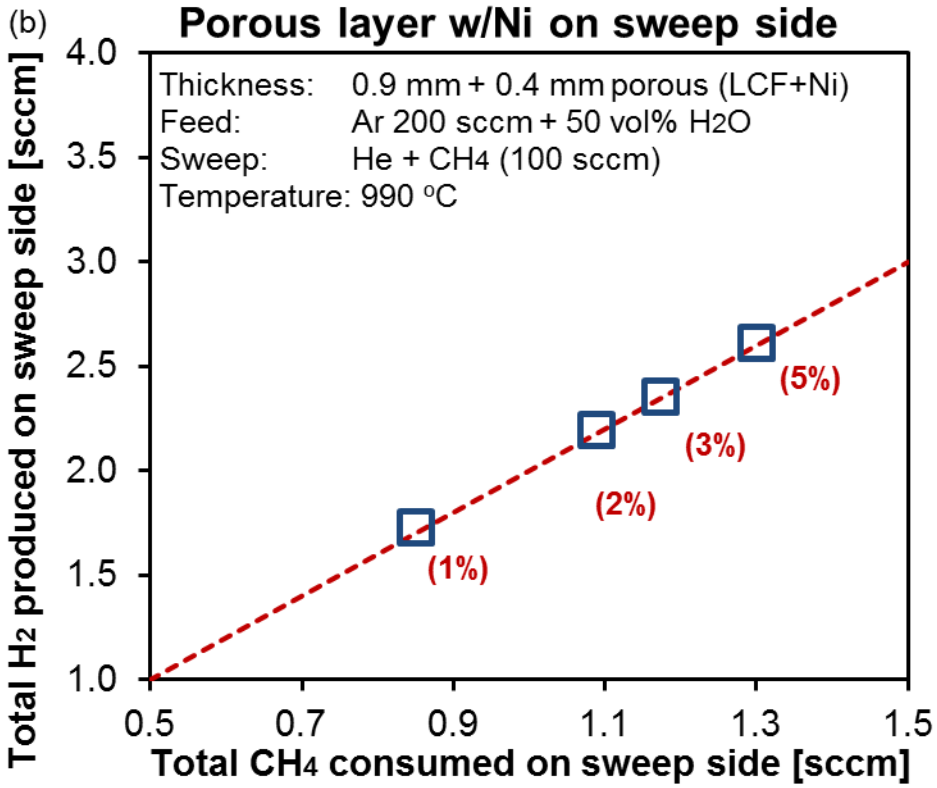

Figure 8 (b) Hydrogen atoms in methane are converted to hydrogen molecules at the outlet of the reactor (The dotted line shows a $n_{H_2} / \Delta n_{CH_4}$ ratio of 2). The numbers in the brackets near the symbols represent the methane concentration at that specific data point. On both figures, the numbers in the brackets near the symbols represent the inlet methane concentration at that specific data point, and $Q"_i$ is the flow rate of species *i* on sweep side under standard condition

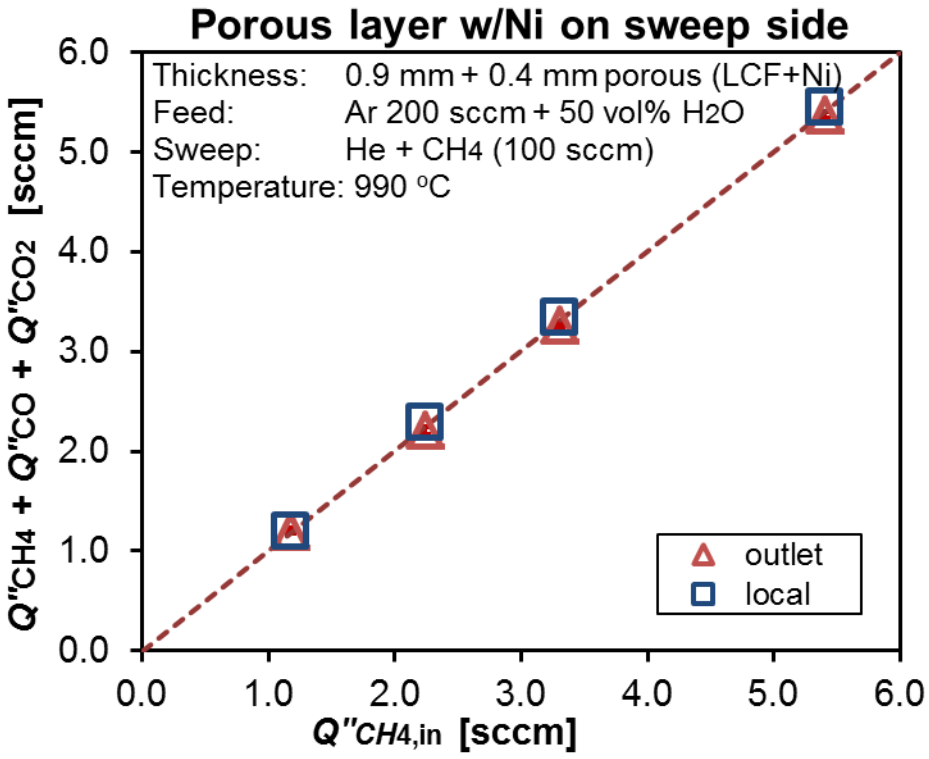

Figure 9 On the sweep side, the gaseous carbon species near the local membrane surface and at the outlet both match well with the inlet carbon species, showing that hardly any solid carbon was formed. $Q"_i$ is the flow rate of species i on sweep side under standard condition

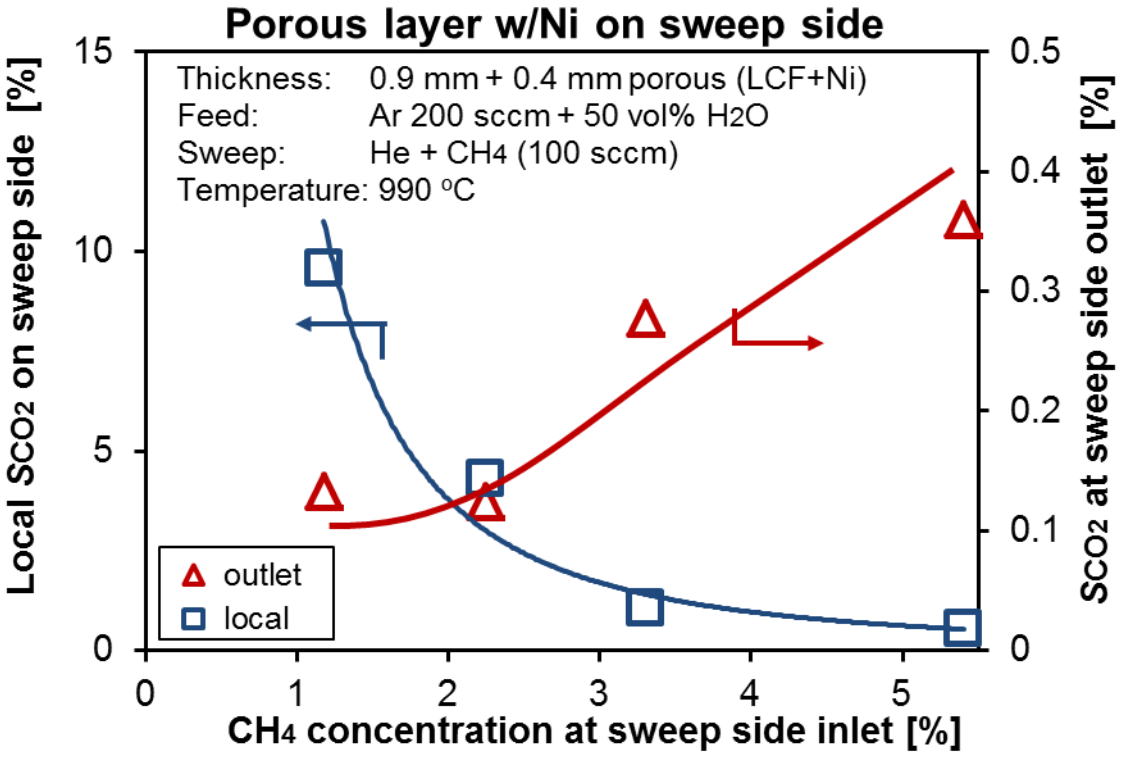

Figure 10 The selectivity to CO_2 is higher near the local membrane surface than that at the outlet. At inlet higher methane concentration, the local CO_2 selectivity decreases